Atmospheric
Measurement
Techniques

Open Access

EGU

Supplement of

Troposphere–stratosphere-integrated bromine monoxide (BrO) profile retrieval over the central Pacific Ocean

Theodore K. Koenig et al.

Correspondence to: Theodore K. Koenig (thekonkoe@ust.hk) and Rainer Volkamer (rainer.volkamer@colorado.edu)

A Instrumentation

A.1 Details of MT-DOAS at MLO

The telescope is located near the southwest corner of Solar Radiation Deck above the NDACC (Network for Detection of Atmospheric Composition Change) building. The primary viewing direction of the telescope is very nearly due northwest, along a free line of sight to the right of the ridge connecting Mauna Loa and Hualalai. Visual inspection indicates the center of the small volcanic cone Pu'u Wa'awa'a (heading -45.9°; relative to north with clockwise positive) is located slightly to the right of the viewing direction, while a high albedo area on the lower slopes of Hualalai west of the lava flow of 1859 (heading -53.2°) is slightly closer but to the left. The viewing direction is estimated to be between these two angles as -50±2°. The EA pointing of the telescope was calibrated through use of a laser level. The absolute pointing is level to better than 0.08° limited by the reproducibility of the laser level. EA pointing is monitored daily through scans across the ridge behind the telescope, and a target located behind the telescope on the deck. These scans indicate that EA pointing is 0.2±0.2° and 0.2±0.1° degrees above horizontal in the primary viewing direction based on target and ridge scan respectively on April 26 and 0.2±0.2° and 0.0±0.2° degrees on April 29. Additionally, we have found that pointing might slowly vary by ±0.2° over the course of a day. Based on these scans, we treat EA pointing on both days as accurate within ±0.2° though it is possible that pointing was very slightly systematically above nominal especially on the 26th.

Based on data from CONTRAST and CINDI-2 it was determined that the placement of the BG3, and BG38 optical filters in close proximity could lead to an etalon (free spectral range ~10 nm, low finesse) which was sensitive to the temperature of the filters (inferred from observed sensitivities to temperatures measured near the filters and to illumination). The optical filters were therefore split up with BG3 left in the optical tube of the telescope. A maintenance trip in January 2020 revealed that the BG3 filter had numerous cracks (presumably from thermal-mechanical stress), however, no change in spectral throughput is obvious between the initial deployment and this date, indicating whenever the cracks occurred they had minimal if any impact. Light collected in the telescope travels to the spectrographs though a series of optical fibers, first a 25m long 1.25µm diameter monofiber coupled at the telescope, then a 12m long 1.5µm diameter mixing fiber, and finally a 1m long 44×145µm fiber bundle which splits from a circular arrangement coupled to the mixing fiber to 38×1 and 8×1 linear arrays aligned on the spectrograph slits. On a roughly monthly basis Hg and Kr lamps are coupled to the mixing fiber (accessible in the building interior) to characterize the instrument line shapes. The 38×1 fiber array was coupled to the AP with a custom 500 grooves mm^{-1} grating rotated to cover a spectral range of 307.6 - 474.8 nm. The spectral resolution was 0.593 nm per full-width at half-maximum (FWHM) based on the Hg emission line at 334.15 nm, and was characterized by quadratics for left-side and right-side width adjustments across the spectrometer. The FWHM varied by less than 2% from that at 334.15 for λ<360 nm and was 0.645 nm for the Hg emission line at 404.66 nm. Because of the extended nature of the deployment the AP operated without a shutter. The 8×1 fiber array was coupled to an Ocean Optics QE65000 spectrometer (QE) with a 300 groove mm^{-1} grating covering the spectral range of 414.3 - 1119.7 nm. The spectral resolution of the QE was 1.45 nm based on the Kr emission line at 450.24 nm and varied less than 1.4% for λ < 575 nm.

1

A.2 Details of AMAX-DOAS

35   For clarity we labelled all CONTRAST campaign profiles sequentially; level flight between monotonic aircraft vertical profiling is included in the same profile such that all ascents are odd-numbered and all descents even numbered. The profiles near Hawaii are RF01-06, -07, and -08. Approaching from the east, the relevant portion of RF01-06 descended over the edge of cloud deck from ~9 km altitude, adjusted heading to roughly parallel with the coast of Hawai'i Island during a level leg, then descended in a series of short broken steps first over the Kohala peninsula then spiralling to a missed approach at Kona

40   (KOA). The reference spectrum was collected during this descent. As demonstrated in Fig. 7, this flight path took the aircraft through air which would be visible to the instrument at MLO at blue wavelengths (such as those NO_2 absorbs at), but does not overlap with the airmasses sampled for the measurement of BrO and HCHO. Nonetheless we do not anticipate strong horizontal gradients in the free troposphere and anticipate a meaningful comparison with data from MLO. RF01-07 following the missed approach ascended continuously first out to the rough midpoint of the Alenuihaha Channel then westward along the path of

45   the channel, then into a trapezoid west of Hawai'i Island. A mostly contiguous and flat cloud deck between ~9.5 km and ~11.0 km altitude required filtering of data in this range. The top of this cloud deck corresponded approximately with the lowest extent of the stratospheric intrusion associated with the RWB. Following a period of level flight starting a square near the previous trapezoid RF01-08 was a nearly continuous descent roughly parallel to the island chain to landing in Honolulu (HOA). The aircraft descended through the same contiguous cloud deck as RF01-07, which again required some filtering. Below ~6

50   km, complex broken cloud fields over Oahu exacerbated by a low sun as dusk approached render the remainder of the descent unusable.

A regular spectral feature interference in the CONTRAST data which had limited the simultaneous accurate fitting of BrO and HCHO has since been identified as an etalon (since eliminated) which it was found could be addressed by including a non-linear pseudo absorber designed to address small changes in spectra resolution. Following these changes, the handling of O_4,

55   and O_3 cross-sections was re-examined seeking among the assessment criteria, consistency with the HCHO profile measured by the In-Situ Airborne Formaldehyde (ISAF) instrument. Further, on the basis of the findings for the MT-DOAS summarized in Fig. 2, the fitting window was extended to start at 328.3 nm (the widest practical for the AMAX-DOAS detector). A number of further changes were made to the starting point, applying the same 3 picometer shift of the Serdyuchenko et al., (2014) cross section used for the MT fitting and adding σ_{O3}^2 in addition to $\lambda \times \sigma_{O3}$ to reproduce the handling of cross-sections in Pukite and

60   Wagner, (2016). From this starting point, the constraint or free-fitting of O_4 and the inclusion or exclusion of a second O_3 cross-section with a temperature of 243 K was examined. The effects of these sensitivities on BrO and HCHO dSCDs are summarized in Fig. S14. In brief, not constraining O_4 leads to fitting more BrO at lower altitudes and a secondary peak in signal around 6 km altitude, and less in the stratospheric intrusion. In notable contrast to the other fit settings, constraining O_4 and not including a second O_3 cross-section does not retrieve large amounts of HCHO in the stratospheric intrusion. Based on

65   comparison with the ISAF derived HCHO profile (Figs. 7 and S14) the second O_3 cross-section was not used going forward. Settings for the optimal estimation retrieval mostly followed those used in Koenig et al., 2017, with some minor modifications.

First, because of the limited information available between 9.5 – 11.5 km due to the cloud deck, the retrieval grid resolution was reduced to 1 km over this range rather than the 500 m used elsewhere. For both BrO and HCHO, the covariance matrix was constructed with 10,000% a priori error; for BrO a 500 m correlation height was used, a 0.5 ppt a priori profile, and SCD_{Ref}

70    $= 2.5 \times 10^{13}$ molec. Cm^{-2}; for HCHO a 1 km correlation with an a priori of 500 ppt below 1.5 km and mixing ratio decreasing exponentially with a folding height of 1 km to 50 ppt, and SCD_{Ref} of 2.7×10^{15} molec. cm^{-2}. These much less constrained settings compared to those used for the MT retrievals reflect the much higher information content of the aircraft measurements. The individual profiles retrieved for RF01-06, -07, and -08, are averaged to a single average profile weighted based on the inverse retrieved uncertainty, with the combined uncertainty propagating the component uncertainties and the variance.

75 **B Albedo, pointing, and directional effects**

While developing the aerosol retrieval for MT-DOAS and testing O_4 fit settings, it was found that the dSCDs of upward looking angles were enhanced when compared to those in both a forward geometry (EA = 0°) and zenith geometry relative to what is modelled in a Rayleigh atmosphere. We conducted sensitivity studies in McArtim to examine effects which we hypothesized could lead to such an effect. We highlight these at 477 nm and using O_4 because of the high signal-to-noise and large dynamic

80   range of SCDs during a typical EA scan, and the longer light-paths enhance the differences among the sensitivity studies and make a number of effects apparent which are not readily observed at 360 nm. These case studies are summarized in Fig. S5. Examining the negative EA, reveals the importance of including such angles in radiative transfer modelling and MT-DOAS retrievals. The forward viewing geometry, which for topographic surface sensors is typically most sensitive to aerosol has only ~1% differences between Rayleigh modelled and measured SCDs when matching zenith measurements, which alone would

85   indicate no need to model aerosol. However, the EA = -1° are modelled in a Rayleigh atmosphere as 2.9×10^{43} molec.^{2} cm^{-5} (34%) higher than measured making clear the existence of additional extinction. Introducing aerosol below the MAX-DOAS reproduces EA = -1°, -2°, and -3° to better than 3×10^{42} molec.^{2} cm^{-5} and better than 5%, while the differences for EA = -4.5° remain significant at ~9.5×10^{42} molec.^{2} cm^{-5} (19%). Inaccurate downward EA pointing makes the measurements of negative angles more difficult to reproduce because the -1° becomes more similar to other negative angles with decreased sensitivity

90   above ~1.9 km and enhanced sensitivity below 1.9 km (Fig. S5 right). This further reinforces that the instrument EA pointing is unlikely to be inaccurate. High albedo enhances the sensitivity of negative EA (like all geometries) to low altitudes, however, this effect is most marked for the zenith geometry which is increased by ~1.8×10^{43} molec.^{2} cm^{-5} compared to ~1.4×10^{43} molec.^{2} cm^{-5} on average for EA < 0°. Accounting for the adjustment of the SCD_{Ref} this would lower the amount of aerosol necessary to match measurements, but as discussed below makes the forward geometry impossible to reproduce without additional

95   effects. One such effect is raising the surface to 3.3 km effectively removing the atmosphere below the instrument which strongly overpowers the albedo effect for downward geometries. This causes downward looking geometries to have SCDs similar to a zenith geometry with a shallow region of sensitivity near the instrument. The failure of the default retrieval to fully reproduce -4.5° might arise from a similar effect. The weighting functions for -4.5° and -3° are very similar and it is challenging

to place aerosol extinction to lower the O_4 SCD of one and not the other. The lightpaths at -4.5º and 477 nm might impact the surface at some large distance or otherwise be impacted by proximity to the terrain; this effect is not clear at 360nm, indicating a possible ranging effect.

Examining the forward and low upward EA box airmass factors demonstrates several surprising coincidences. For the forward geometry, the -0.3º EA cases have enhanced sensitivity to the instrument altitude relative to the Rayleigh case, but decreases at higher altitudes as the aerosol retrieval must add aerosol to compensate for this. Inaccurate pointing can improve the comparison with measurements for low upward EA, and with albedo effects can bound it. Only increasing albedo raises forward O_4 dSCD relative to the nearest zenith by ~9.2×10^{42} molec.^{2} cm^{-5} (9%). This is significantly worse agreement than the Rayleigh or default cases which both agree within 1.7×10^{42} molec.^{2} cm^{-5} (1.6%). An albedo of ~0.5 together with an elevated surface (not shown) can fully reproduce forward and low upward EA. However, negative angles and pointing tests indicate that pointing is accurate to within 0.2º and likely better. From prior experience increased aerosol single scattering albedo can create similar effects and we expect better reflects reality. However, the solution is highly under constrained. This effect is more muted at 360 nm to the point that differences are not significant within measurement uncertainty on average. Examining the box airmass factors for EA 3º shows that for all cases apart for the dull elevated surface they are enhanced above the instrument relative to Rayleigh. The base case is quite similar to a Rayleigh atmosphere above the instrument, however, as is visible in the left panel it has a slightly greater SCD for O_4 from the sensitivity below the instrument. The same is not necessarily the case for BrO or other trace gasses with a different profile shape, demonstrating the need to consider geometries, such as the previously discussed downward EA, simultaneously in making use of the constraint of aerosol state provided by O_4 or other means.

More upward looking angles are especially relevant to this work because larger than expected BrO dSCDs at $8º \leq EA \leq 45º$ compared to a zenith geometry in a Rayleigh atmosphere. Looking at these geometries in the left panel of Fig. S5 the elevated high albedo surface performs slightly better than the base case (0.7×10^{42} molec.^{2} cm^{-5}; 3% vs 1.70×10^{42} molec.^{2} cm^{-5}; 4%) for these angles alone, but as previously noted cannot reproduce other angles and these changes are within uncertainty . The source of the O_4 signal is not the same as demonstrated by the box air mass factors for EA = 20º on the right. The sensitivity to altitudes below 4 km in the base case is 66% greater than in the elevated high albedo case. The presence of aerosol enhances sensitivity relative to Rayleigh for all these altitudes. The elevated high-albedo case lacks the lower altitudes entirely but has a much large enhancement relative to the Rayleigh base case. Comparing to the forward geometry (which is similar for the two cases) the base case EA 20º has greater sensitivity than forward from ~7 km up, while for the elevated high-albedo case this is closer to 6 km. Overall, the elevated albedo case while similarly reproducing O_4 SCDs concentrates sensitivity (and thereby inferred information content) relatively close to the instrument altitude being entirely blind to altitudes below the instrument and lowering the altitude of differential sensitivity above the instrument.

Increasing surface albedo can facilitate reproduction of O_4 in aerosol retrievals and can be especially valuable when using radiative transfer models which don't readily represent a detector aloft. However, users should be mindful, that the results are at least partly spurious. We made use of this effect in retrieving the NO_2 profiles for BrO constraint, as we are only seeking to

scale dSCDs from 477 nm to 360 nm, we believe the method to be sufficiently accurate. We expect that a representation of the "ghost column" of O_4 and/or trace gas below the instrument even roughly estimated would be a better approach when modelling

135 a detector aloft is not an option. Further characterization of the range of such "ghost columns" under varied conditions beyond the sensitivity studies here are needed for this application. Representation of a detector aloft and simultaneous consideration of the full range of geometries accessible is the best approach to use if practical.

As noted in the main text we have excluded a subset of angles from the retrieval, namely those in the reverse direction. In brief, we expect that given the altitude of MLO, that aerosol above the instrument should be reasonably homogeneous.

140 However, we did not retrieve similar aerosol profiles. We expect that this reflects a failure to accurately represent the mountain slope in the upslope geometry. For the days examined the earlier scans present the greatest discrepancy, we note that the upslope direction facing south-east means backward looking angles point in the direction of the solar disk in the morning. Further for SZA = 70º (solar elevation 20º) the angles can bound the solar disk in elevation also. Mauna Loa physically blocks many otherwise valid scattering geometries, but generally only scattering below the peak altitude of ~4.17 km. Being roughly

145 conical we would expect the range of blocked geometries to scale roughly linearly below this altitude. In principle, this effect is similar to that observed in the forward direction for EA = -4.5º at 477 nm. However, facing away from the sun, backscattering is relatively unlikely to interact with terrain. We have not yet represented this selective blocking of light paths in the radiative transfer model and leave these angles out of the analysis. The naïve 3-D approach is expected to be computationally expensive and therefore a 2-D or better yet 1-D approximation is highly preferable.

150 **C Time-dependent retrieval construction**

Setting up the time dependent retrieval required choosing the time dependence function $f(t)$, determining atmospheric layers L with corresponding weights $\mathbf{W^L}$ and a priori values for the corresponding scaling factors $\mathbf{C^L}$. We examine these in this order. As noted in the main text, SZA = 70º was chosen as the reference for $f(t)$ prior to further examination. Two forms of $f(t)$ were examined, both meet the criteria that $f(t) = 0$ at SZA = 70º and $f(t) = 1$ at for the latest measurement included on April 29. The

155 first was a linear function which had negative values for SZA > 70º, while the later is zero for SZA > 70º. The latter is based on time-dependent measured O_3 VCDs (Fig. S10). Using the linear form of $f(t)$ was similarly systematically tested for all $\mathbf{C^L}$ as described below, however, this systematic examination did not identify solution which improved retrieval residual RMS to the same degree, limited primarily by ZS data. This was driven by increased residuals at the highest SZA which already have the largest residuals and are also strongly leveraged by this form of $f(t)$. These same issues might impact any time-dependent

160 retrieval even if the time-dependence is accurate, which may present a challenge to future applications. For the present case, time-independent ZS residuals do not show a discernible trend and we expect the ramp function is more likely to address the observed limitations of the time-independent retrieval and choose this for $f(t)$.

$\mathbf{W^L}$ we constructed on the basis of CAM-Chem, which modelled changes in Br_y and BrO fields on April 29, albeit offset by 4-6 hours from those observed. This time mismatch makes comparison of BrO fields impractical given the rapid photochemical

5

165 repartitioning (which should be partly accounted for by photochemical corrections to AMF in any case). As such we searched for Br_y column enhancements or the movement Br_y between layers in the model. This identified two key processes, the movement of Br_y from the stratosphere to the troposphere as part of the RWB event and the movement of a Br_y layer from below to above 6 km altitude and its simultaneous increase. At first, expecting the RWB to be relevant primarily in the upper troposphere we first defined two atmospheric layers from 2 – 10 km and 10 – 17.4 km. Using these two layers provides overall

170 similar retrieval RMS residual of 6.0×10^{12} molec. cm^{-2} overall, performing slightly worse for ZS data with 7.9×10^{12} molec. cm^{-2}, but better for MAX data with 3.6×10^{12} molec. cm^{-2}. However, the latter statistic obscures that data for EA $\geq$ 12º have systematically more positive residuals while those with EA $\leq$ 0º have systematically more negative residuals. On that basis the bottom layer split at 6 km. Furthermore, the lowermost layer was extended to the surface (despite limited sensitivity) and the stratosphere was added as a layer.

175 Preliminary investigations found that the time-dependent retrieval was highly dependent on the a priori values of the scaling factors $\mathbf{C^L}$, not finding literature on this sensitivity we chose to sample the possible permutations of values systematically. Ideally, retrievals should be relatively insensitive to the choice of a priori. We also thought it possible that the layer scaling a priori sensitivity coupled to the choice of profile a priori via Eq. 5. We chose as the first criterion that for a choice of $\mathbf{C^L}$ the results should be consistent for different choices of a priori BrO profiles. Preliminary investigations found that the retrieved

180 profiles at time zero (SZA = 70º) were relatively similar. While time-dependence is included, some indication of this is given in Fig. S10. We sampled factors $\mathbf{C^L}$ on [-1, 1] every 0.1, it was found that a priori values of 0 produced mathematical singularities. For the remaining 160,000 permutations it was found that only 129 met the criterion that the retrieved partial columns in all layers L vary by less than 2×10^{13} molec. cm^{-2} among the a priori BrO profiles used. These and the the twenty best performing settings are highlighted in Fig. S12. Examining the selected settings, choices for C^{LT} = 0.2 and C^{St} = -0.1 were

185 identified. Subsequently, it was decided that an ideal choice for $\mathbf{C^L}$ a priori should not be strongly sensitive to small changes. Among the limited remaining solution space six solution we found on $C^{MT} \in$ [-0.7, -0.6] and $C^{UT} \in$ [-0.5, -0.3], from which the lowest RMS setting of C^{LT} = 0.2, C^{MT} = -0.7, C^{UT} = -0.4, and C^{St} = -0.1 was selected. For this solution it was found that the stratosphere continued to be a source of instability and given the trend to lower RMS nearer zero for C^{St} in Fig. S13 it was changed to -0.05 for the final analysis.

190 **D Sensitivity studies assessing the uncertainty of fit constraints on BrO dSCDs**

We first examine the effect of individual trace gas constraints on BrO dSCDs in more detail. The O_4 constraint changes BrO dSCDs by an average and standard deviation of $+0.7\pm4.4\times10^{12}$ molec. cm^{-2}, less than the average fit uncertainty of 6.1×10^{12} molec. cm^{-2} and smaller on an individual basis in almost all instances. For ZS fits, the effect is somewhat larger ($-1.1\pm5.4\times10^{12}$ molec. cm^{-2}) but proportionally still smaller than the average fit uncertainty (10.0×10^{12} molec. cm^{-2}). On average, the NO_2

195 constraint counteracts the O_4 constraint but with less variability ($-0.7\pm2.2\times10^{12}$ molec. cm^{-2} effect on BrO dSCDs). The changes while small systematically affect specific EAs with EA$\leq$0° mostly increased by 1-2×10^{12} molec. cm^{-2} and EA=30° typically

decreased by a similar amount. Hence, while less than fit uncertainty in almost all instances, the NO$_2$ constraint can ultimately impact the BrO profile retrieval.

The top panels of Fig. S6 illustrate the importance of the HCHO constraint. Based on the a posteriori HCHO SCDs, the impact of the "drift" in the HCHO-BrO spectral cross-talk varies to as much as ~5×10^{15} molec. cm^{-2} HCHO at SZA = 70° on Apr 26 and is relatively constant around ~1×10^{16} molec. cm^{-2} HCHO on Apr. 29. Applying the constraint of HCHO lowers the HCHO dSCDs by these corresponding amounts and consequently increases BrO. The magnitude of the cross-talk varies, but for this drift BrO dSCDs roughly increase by 2×10^{-3} of the corresponding HCHO decrease, i.e. the ~1×10^{16} molec. cm^{-2} HCHO dSCD decrease on Apr. 29 corresponds to ~2×10^{13} molec. cm^{-2} BrO increase. The effect of the HCHO constraint – including fast and "drift" components – is 1.5±0.9×10^{13} molec. cm^{-2}, dominating the overall effect of the constraints which have the same mean and standard deviation.

We next examine the effect of incorporating these constraints as part of an expanded measurement covariance in the time-independent BrO profile retrieval as well as the BrO cross-section uncertainty. Applying the fit constraints leverages observed information (from other fitting windows and inversions) and cross-section uncertainty are systematic rather than random, as such we do not use them in the default retrieval. We first consider the BrO cross-section uncertainty and the O$_4$ and NO$_2$ constraints. The major features of the retrieved profiles are retained and the changes in BrO VCD are minimal: (-0.2 and -1.0)×10^{12} molec. cm^{-2} on Apr 26 and 29 respectively. The larger effect on Apr 29 is mostly the result of smoothing the profile shape at a lower concentration below ~7.4 km. The reduced signal to noise is reflected as a decrease in DoF by 0.61 on Apr 26 and 0.56 on Apr 29 with each day retaining 4.99 and 5.00 DoF respectively. The loss of DoF is minimal near instrument altitude and is greatest in the uFT and stratosphere. Next we further account for the much larger effect of the HCHO constraint. As expected the effect on Apr 26 is small, with the profile smoothing toward the a priori, a decrease to 4.77 DoF, and a change in BrO VCD of <0.1×10^{12} molec. cm^{-2} compared to the default retrieval. Even on Apr 29 when the effect of the "drift" is greater than many individual dSCDs, 3.87 DoF are still retrieved with almost all the loss from the troposphere where the change in signal to noise is greater. Nonetheless, the change in BrO VCD is still small (-0.9×10^{12} cm^{-2}) and the elevated BrO in the upper troposphere is still retrieved.

References

Bogumil, K., Orphal, J., Homann, T., Voigt, S., Spietz, P., Fleischmann, O. C., Vogel, A., Hartmann, M., Kromminga, H., Bovensmann, H., Frerick, J., and Burrows, J. P.: Measurements of molecular absorption spectra with the SCIAMACHY pre-flight model: instrument characterization and reference data for atmospheric remote-sensing in the 230–2380 nm region, J. Photochem. Photobiol. A Chem., 157, 167–184, https://doi.org/10.1016/S1010-6030(03)00062-5, 2003.

Dix, B., Koenig, T. K., and Volkamer, R.: Parameterization retrieval of trace gas volume mixing ratios from Airborne MAX-

DOAS, Atmos. Meas. Tech., 9, 5655–5675, https://doi.org/10.5194/amt-9-5655-2016, 2016.

230   Finkenzeller, H. and Volkamer, R.: O2–O2 CIA in the gas phase: Cross-section of weak bands, and continuum absorption between 297–500 nm, J. Quant. Spectrosc. Radiat. Transf., 279, 108063, https://doi.org/10.1016/J.JQSRT.2021.108063, 2022.

Fleischmann, O. C., Hartmann, M., Burrows, J. P., and Orphal, J.: New ultraviolet absorption cross-sections of BrO at atmospheric temperatures measured by time-windowing Fourier transform spectroscopy, J. Photochem. Photobiol. A

235   Chem., 168, 117–132, https://doi.org/10.1016/J.JPHOTOCHEM.2004.03.026, 2004.

Koenig, T. K., Volkamer, R., Baidar, S., Dix, B., Wang, S., Anderson, D. C., Salawitch, R. J., Wales, P. A., Cuevas, C. A., Fernandez, R. P., Saiz-Lopez, A., Evans, M. J., Sherwen, T., Jacob, D. J., Schmidt, J., Kinnison, D., Lamarque, J.-F., Apel, E. C., Bresch, J. C., Campos, T., Flocke, F. M., Hall, S. R., Honomichl, S. B., Hornbrook, R., Jensen, J. B., Lueb, R., Montzka, D. D., Pan, L. L., Reeves, J. M., Schauffler, S. M., Ullmann, K., Weinheimer, A. J., Atlas, E. L.,

240   Donets, V., Navarro, M. A., Riemer, D., Blake, N. J., Chen, D., Huey, L. G., Tanner, D. J., Hanisco, T. F., and Wolfe, G. M.: BrO and Br_y profiles over the Western Pacific: Relevance of Inorganic Bromine Sources and a Br_y Minimum in the Aged Tropical Tropopause Layer, Atmos. Chem. Phys., 17, 15245–15270, https://doi.org/10.5194/acp-2017-572, 2017.

Kraus, S.: DOASIS A Framework Design for DOAS, University of Mannheim, 2006.

245   Meller, R. and Moortgat, G. K.: Temperature dependence of the absorption cross sections of formaldehyde between 223 and 323 K in the wavelength range 225-375 nm, J. Geophys. Res. Atmos., 105, 7089–7101, https://doi.org/10.1029/1999JD901074, 2000.

Pukite, J. and Wagner, T.: Quantification and parametrization of non-linearity effects by higher-order sensitivity terms in scattered light differential optical absorption spectroscopy, Atmos. Meas. Tech., 9, 2147–2177,

250   https://doi.org/10.5194/AMT-9-2147-2016, 2016.

Rothman, L. S., Gordon, I. E., Barber, R. J., Dothe, H., Gamache, R. R., Goldman, A., Perevalov, V. I., Tashkun, S. A., and Tennyson, J.: HITEMP, the high-temperature molecular spectroscopic database, J. Quant. Spectrosc. Radiat. Transf., 111, 2139–2150, https://doi.org/10.1016/J.JQSRT.2010.05.001, 2010.

Serdyuchenko, A., Gorshelev, V., Weber, M., Chehade, W., and Burrows, J. P.: High spectral resolution ozone absorption

255   cross-sections – Part 2: Temperature dependence, Atmos. Meas. Tech, 7, 625–636, https://doi.org/10.5194/amt-7-625-2014, 2014.

Siddans, R.: Personal Communication, 2023.

Thalman, R. and Volkamer, R.: Temperature dependent absorption cross-sections of O_2-O_2 collision pairs between 340 and 630 nm and at atmospherically relevant pressure, Phys. Chem. Chem. Phys., 15, 15371–81,

260   https://doi.org/10.1039/c3cp50968k, 2013.

Vandaele, A. C., Hermans, C., Simon, P. C., Carleer, M., Colin, R., Fally, S., Mérienne, M. F., Jenouvrier, A., and Coquart, B.: Measurements of the NO_2 absorption cross-section from 42 000 cm^{-1} to 10 000 cm^{-1} (238–1000 nm) at 220 K

and 294 K, J. Quant. Spectrosc. Radiat. Transf., 59, 171–184, https://doi.org/10.1016/S0022-4073(97)00168-4, 1998.

265

Table S1. Mountaintop MAX-DOAS fitting windows.

| Fitting Window	Wavelength range	Absorber	Comments; References
$O_{4,uv}$	350 – 388 nm	O_4	300 K; (Finkenzeller and Volkamer, 2022)
		O_3	223 K and 243 K, , 243 K cross-section is orthogonalized to 223 K cross-section; (Serdyuchenko et al., 2014)†
		NO_2	220 K; (Vandaele et al., 1998)
		HCHO	293 K; (Meller and Moortgat, 2000)
		BrO	223 K; (Fleischmann et al., 2004)
		Rotational Raman	250 K cross-section and $\lambda \times$ cross-section; (Kraus, 2006)
	6th order polynomial and linear intensity offset		
Visible	425 – 490 nm	O_4	293 K; (Thalman and Volkamer, 2013)
		NO_2	298 K and 220 K, 220 K is orthogonalized to 298 K; (Vandaele et al., 1998)
		H_2O	298 K, HITEMP 2010; (Rothman et al., 2010)
		O_3	223 K; (Serdyuchenko et al., 2014)
		Rotational Raman	250 K; (Kraus, 2006)
	4th order polynomial and linear intensity offset		
HCHO	328.5 – 359 nm	HCHO	293 K; (Meller and Moortgat, 2000)
		O_4	300 K, 344 nm and 328 nm bands scaled by 0.80 based on empirical fit fixed to results from O_4 window; (Finkenzeller and Volkamer, 2022)
		O_3	223 K and 243 K;, 243 K cross-section is orthogonalized to 223 K cross-section; (Serdyuchenko et al., 2014)†
		NO_2	220 K fixed to simulated values using weighting functions derived from O_4 in the $O_{4,uv}$ after inversion using Visible window O_4 and NO_2; (Vandaele et al., 1998)
		BrO	223 K; (Fleischmann et al., 2004)
		Rotational Raman	250 K cross-section and $\lambda \times$ cross-section; (Kraus, 2006)
	6th order polynomial and linear intensity offset		
BrO	328.5 – 359 nm	BrO	223 K; (Fleischmann et al., 2004)
		O_4	300 K, 344 nm and 328 nm bands scaled by 0.80 based on empirical fit fixed to results from O_4 window; (Finkenzeller and Volkamer, 2022)
		O_3	223 K and 243 K, , 243 K cross-section is orthogonalized to 223 K cross-section; (Serdyuchenko et al., 2014)†
		NO_2	220 K, fixed to simulated values using weighting functions derived from O_4 in the $O_{4,uv}$ after inversion using Visible window O_4 and NO_2; (Vandaele et al., 1998)
		HCHO	293 K; (Meller and Moortgat, 2000)
		Rotational Raman	250 K cross-section as well as $\lambda \times$ cross-section both used; (Kraus, 2006)
	6th order polynomial and linear intensity offset		

† Shifted by 3 pm per the recommendation in (Siddans, 2023)

Table S2. CU AMAX-DOAS fitting windows.

Fitting Window	Wavelength range	Absorber	Comments; References
$O_{4,uv}$	350 – 388 nm	O_4	293 K; (Thalman and Volkamer, 2013)
		O_3	223 K; (Serdyuchenko et al., 2014)†
		NO_2	220 K; (Vandaele et al., 1998)
		HCHO	293 K; (Meller and Moortgat, 2000)
		BrO	223 K; (Fleischmann et al., 2004)
		Rotational Raman	250 K cross-section as well as $\lambda \times$ cross-section both used; (Kraus, 2006)
	5th order polynomial and linear intensity offset		
UV	332.3 – 359 nm	BrO	223 K; (Fleischmann et al., 2004)
		HCHO	293 K; (Meller and Moortgat, 2000)
		O_4	293 K, scaled by $(350/360)^4$ assuming Rayleigh scattering; (Thalman and Volkamer, 2013)
		O_3	223 K,; (Serdyuchenko et al., 2014)†
		NO_2	220 K; (Vandaele et al., 1998)
		Rotational Raman	250 K cross-section as well as $\lambda \times$ cross-section both used; (Kraus, 2006)
	6th order polynomial and linear intensity offset		

270   † Shifted by 3 pm per the recommendation in (Siddans, 2023)
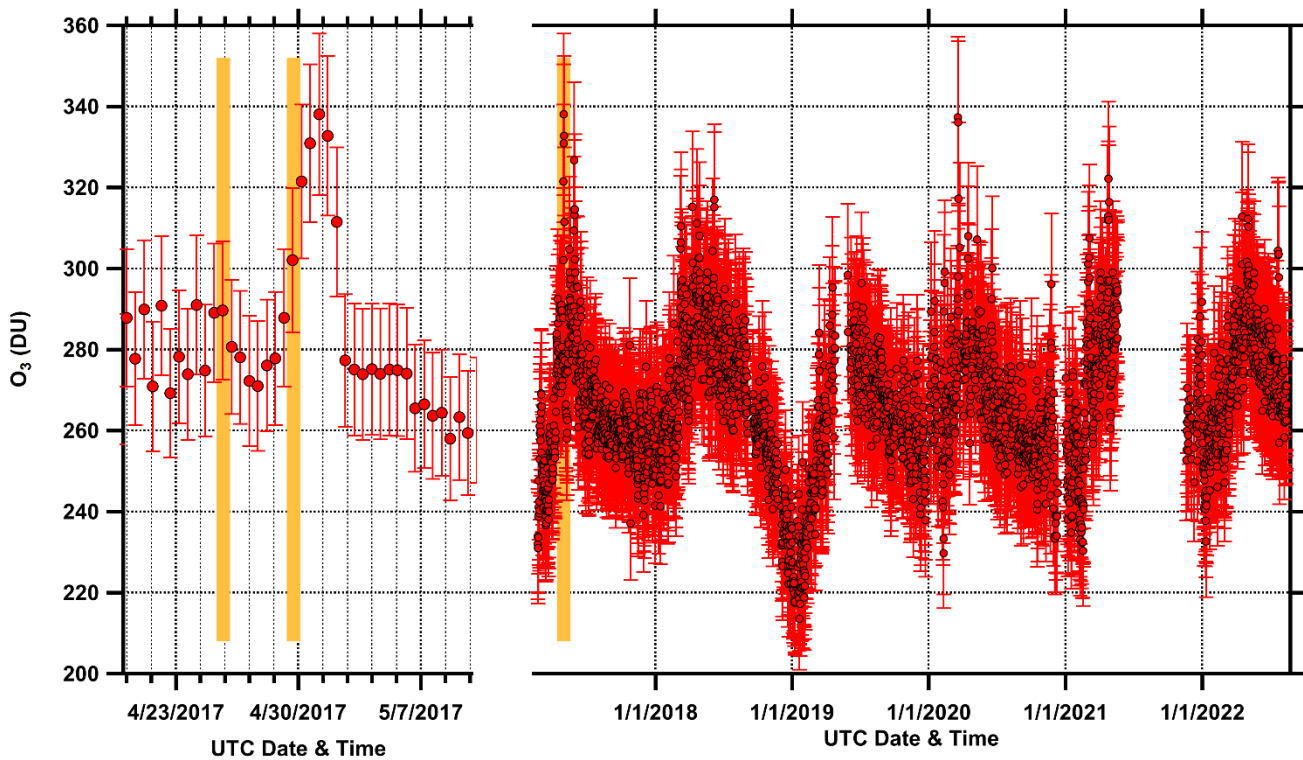
Figure S1: NDACC retrievals of O₃ VCDs

Routine NDACC retrieved O₃ VCDs using ZS data collected each dawn and dusk. Left: late April to early May 2017, the mornings of April 26 and 29, 2017 (which nearly overlap with midnight UTC) analyzed in this work are highlighted, cloud conditions on April 30 and May 1 preclude the use of MAX data on those days. Right: data from February 2017 to August 2022, April 2017 is highlighted. In the course of five years, the only other RWB similar in magnitude based on O₃ was detected is in March 2020.

275
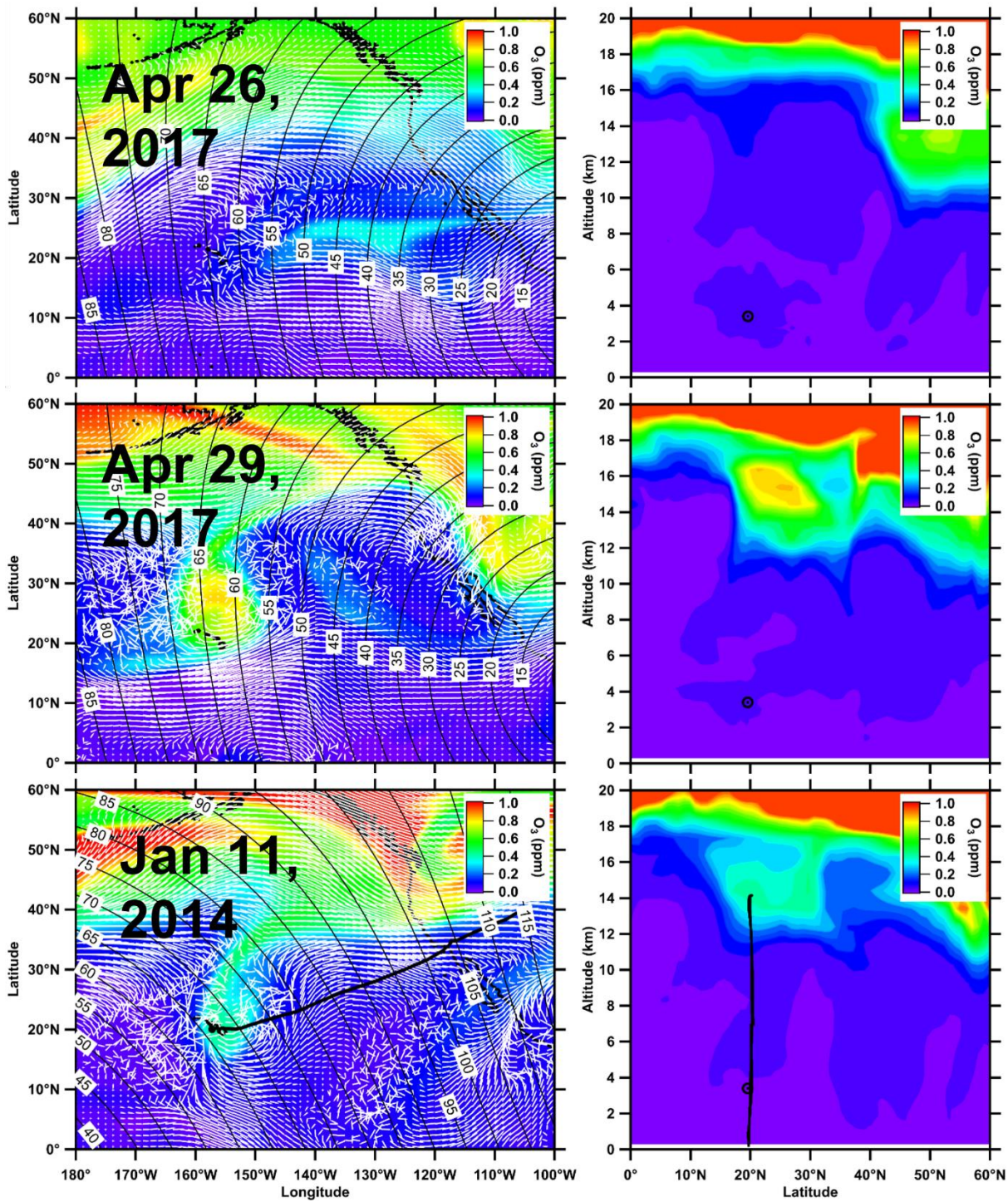
Figure S2: Overview of atmospheric and observation conditions for case studies

Left: O₃ from CAM-Chem at 14 km altitude arrows show zonal winds and contours show SZA. Right: O₃ curtains at 160ºW.
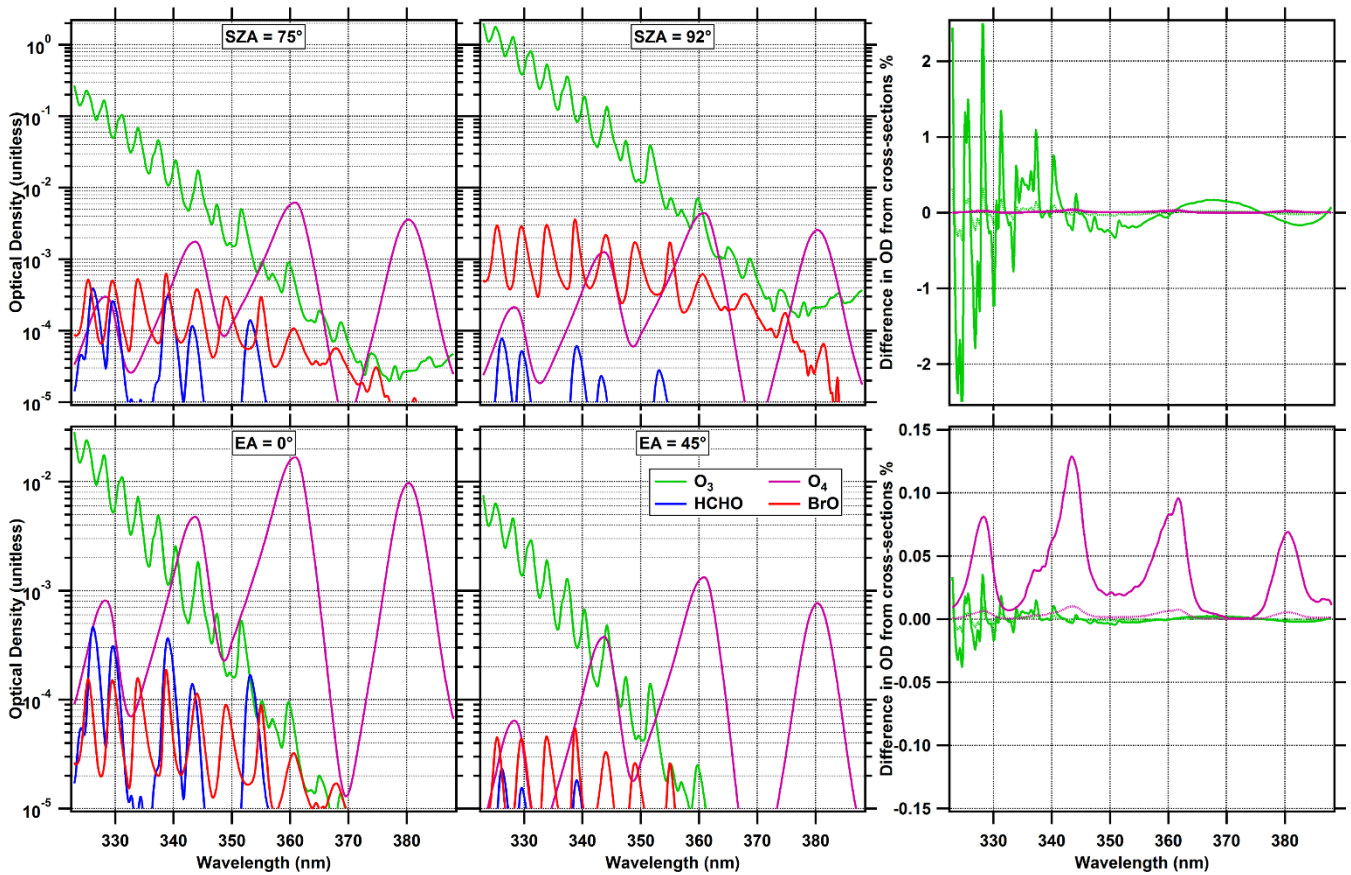
Figure S3: Typically observed optical densities for different observation geometries

Top row: ZS data. O_3 and O_4 are more optically thick than BrO at SZA = 75°, the latter is mitigated at SZA = 92°. the OD of O_3 is a factor of ~2 that of BrO at 359 nm, but over 100 times more optically thick below 330 nm. Bottom row: MAX data. HCHO is additionally important, especially for EA = 0°. Right: differences in optical density resulting from the choice of cross-section, for O_3 (Serdyuchenko et al., 2014) **compared to** (Bogumil et al., 2003) **after orthogonalization to a cubic polynomial (as processed for fitting), for O_4 (Finkenzeller and Volkamer, 2022) compared to (Thalman and Volkamer, 2013). Solid lines correspond to the larger OD (SZA = 92° and EA = 0°) while the dashed lines correspond to the lesser OD (SZA = 75° and EA = 45°).**
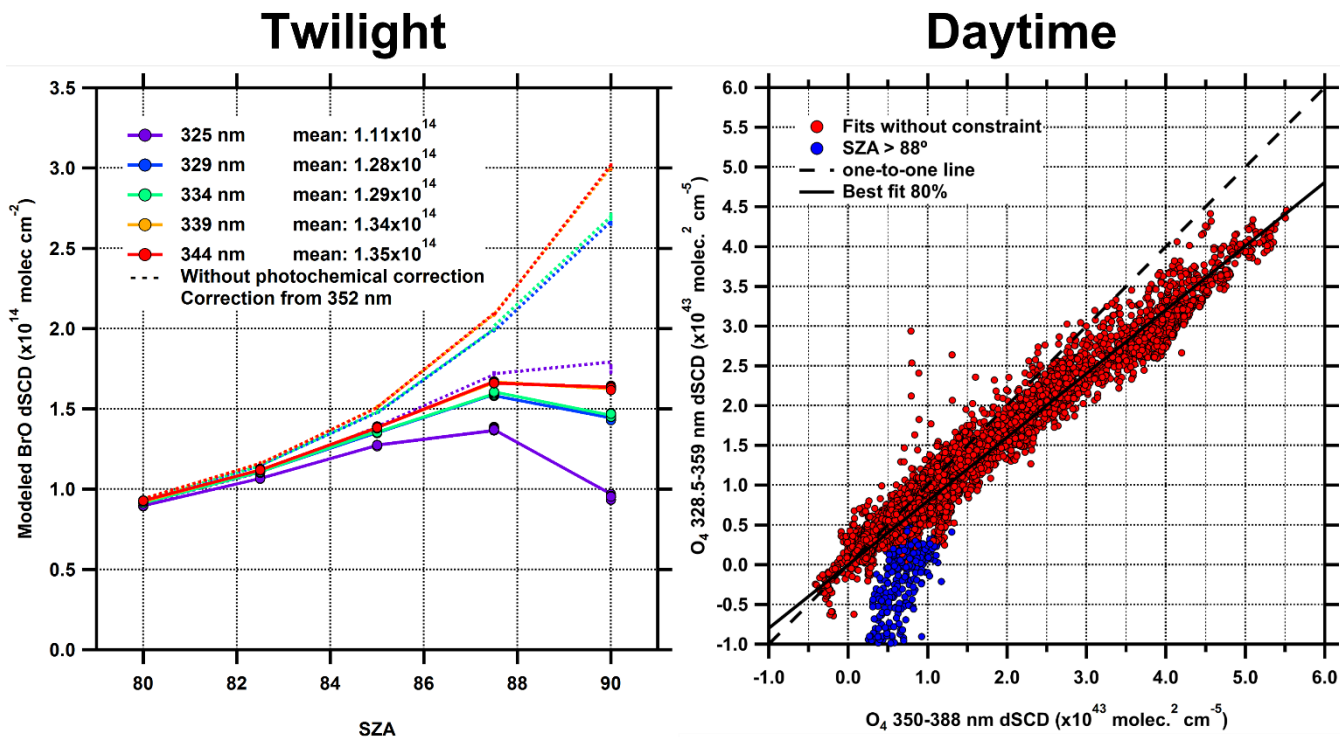
Figure S4: Assessment of spectral interferences for BrO fitting

Left: The BrO dSCD is modelled in detail at 0.1 nm resolution under twilight conditions for a variety of SZA and SRAA (effect is almost imperceptible). When accounting for photochemical changes at twilight BrO varies by ~50% for $80° <$ SZA $< 90°$ and are consistent for different BrO bands apart from the 325 nm band. Right: correlation of O_4 fitted in the BrO and HCHO fitting window against the O_4-optomized fitting window. For SZA $< 88°$, fits follow a correlation line of 0.80 despite significant scatter. For final fit settings O_4 is then constrained to value fitted in the O_4 – optimized window scaled by this factor.
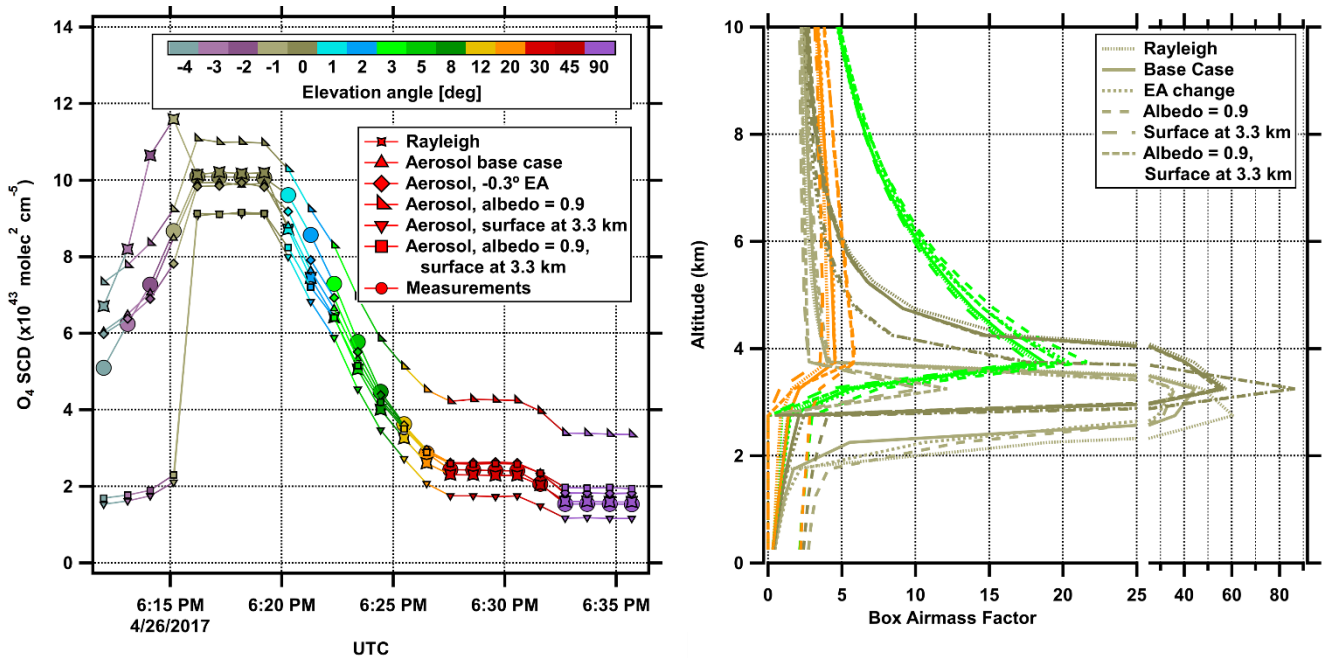
Figure S5: Radiative transfer sensitivity studies at 477 nm examining the effects of inaccurate EA pointing, albedo and terrain

Left: O₄ SCDs modelled for a Rayleigh atmosphere, using the default settings of a surface at 0 km altitude with and albedo 0.08, as the base case but lowering all angles by 0.3º, with bad pointing and a surface albedo of 0.9, as the base case but with the surface raised to 3.3 km altitude, and the base case, but with the surface at 3.3 km and with albedo of 0.9. All modelled SCDs are compared to the measurements for the third scan on April 26, 2017. Right: The box airmass factors for EA = -1º, 0º, 3, and 20ºcolor coded as on the left. The line styles indicate the different model cases.

17
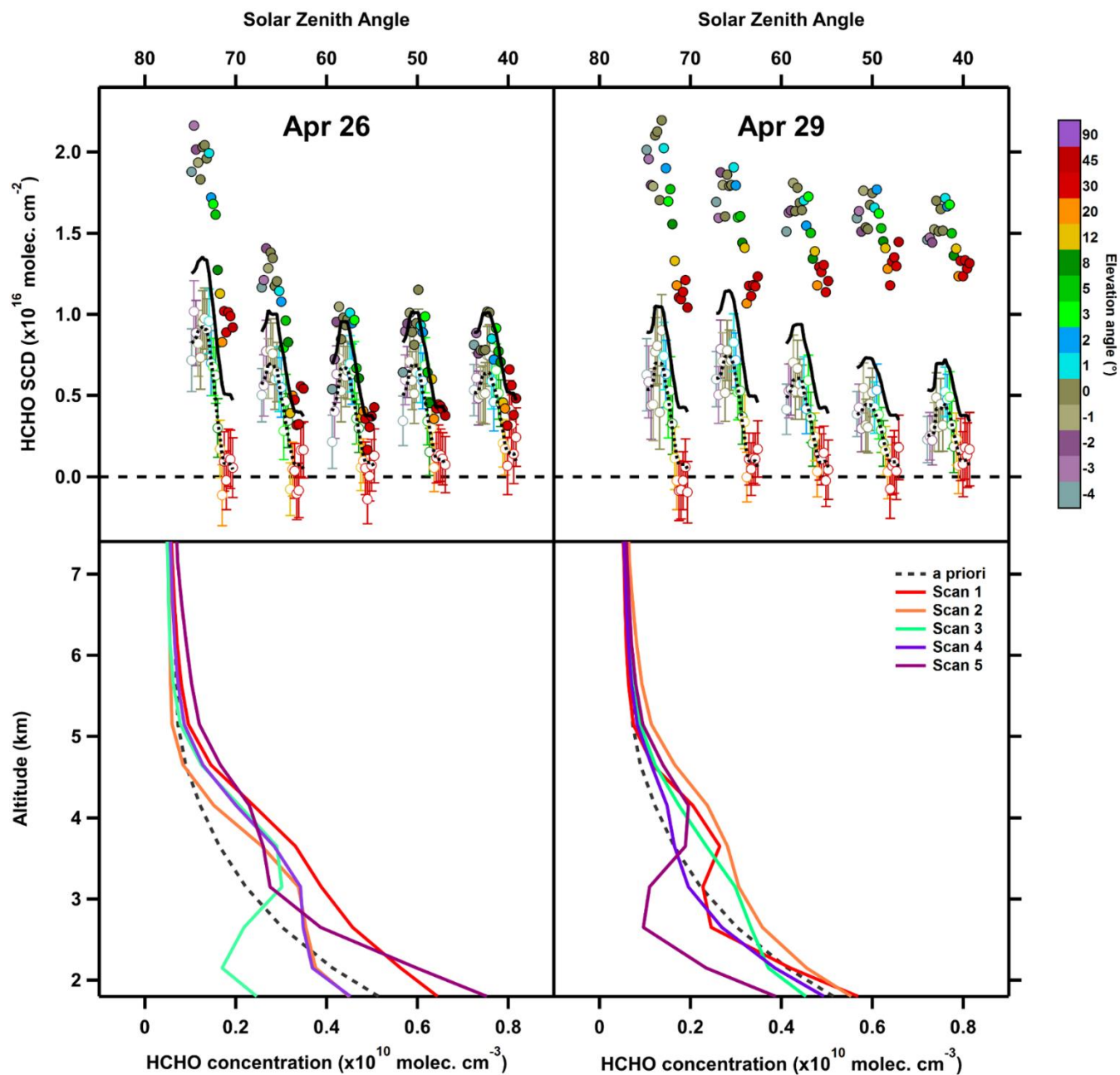
315 **Figure S6: MT-DOAS HCHO retrieval**

Top: in solid circles SCDs using fixed-reference analysis, in open circles dSCDs using a moving reference analysis. These dSCDs are used in conjunction with differential weighting function to retrieve the profiles in the lower panels. The modelled dSCDs in dashed black are used to constrain the BrO fitting. In solid black the modelled HCHO SCDs by adding SCD_{Ref}, which for later scans

on April 26 (closer to the fixed reference) closely follow the measured SCDs. Bottom: retrieved HCHO profiles. For each day scans

320 are numbered sequentially and retrieved separately.
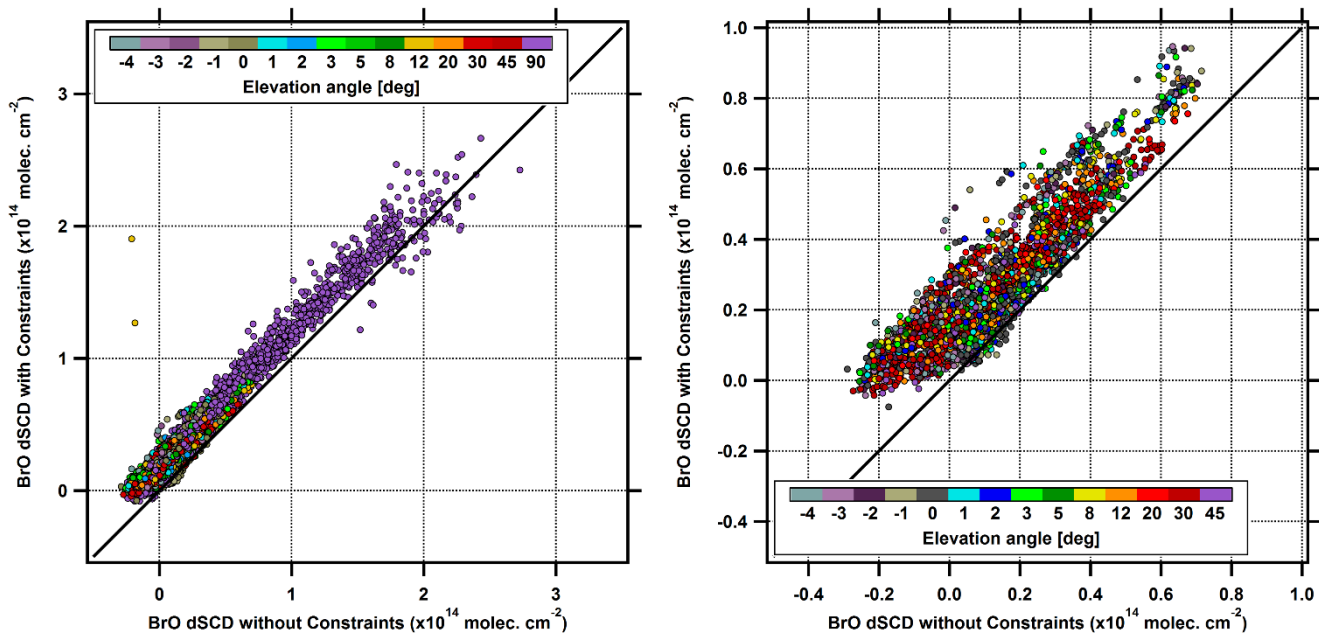
Figure S7: Effects of spectral constraints on BrO dSCDs

Left: ZS and MAX data for April 26 and April 29. Right: MAX data only with smaller range. Black line shows 1:1 line.
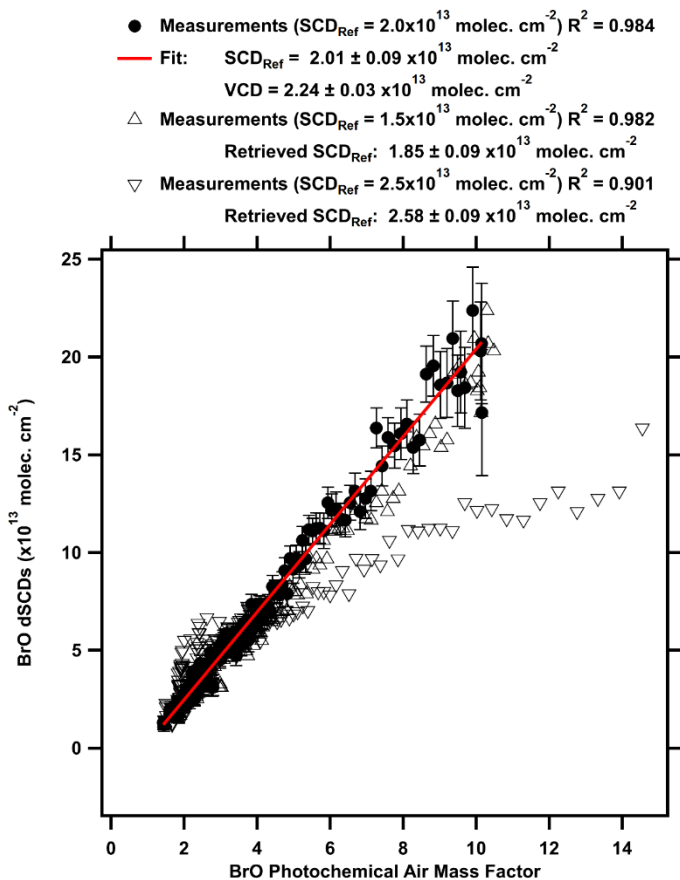
Figure S8: Photochemical Langley Plot for BrO

The photochemical AMF accounts for longitudinal changes in Br_y partitioning along the line of sight changing BrO which is most relevant at larger SZA (and therefore larger AMF). Using $SCD_{Ref} = 2.0 \times 10^{13}$ molec. cm^{-2} recovers itself and has the best fit, while other initial values of SCD_{Ref} do not recover themselves.
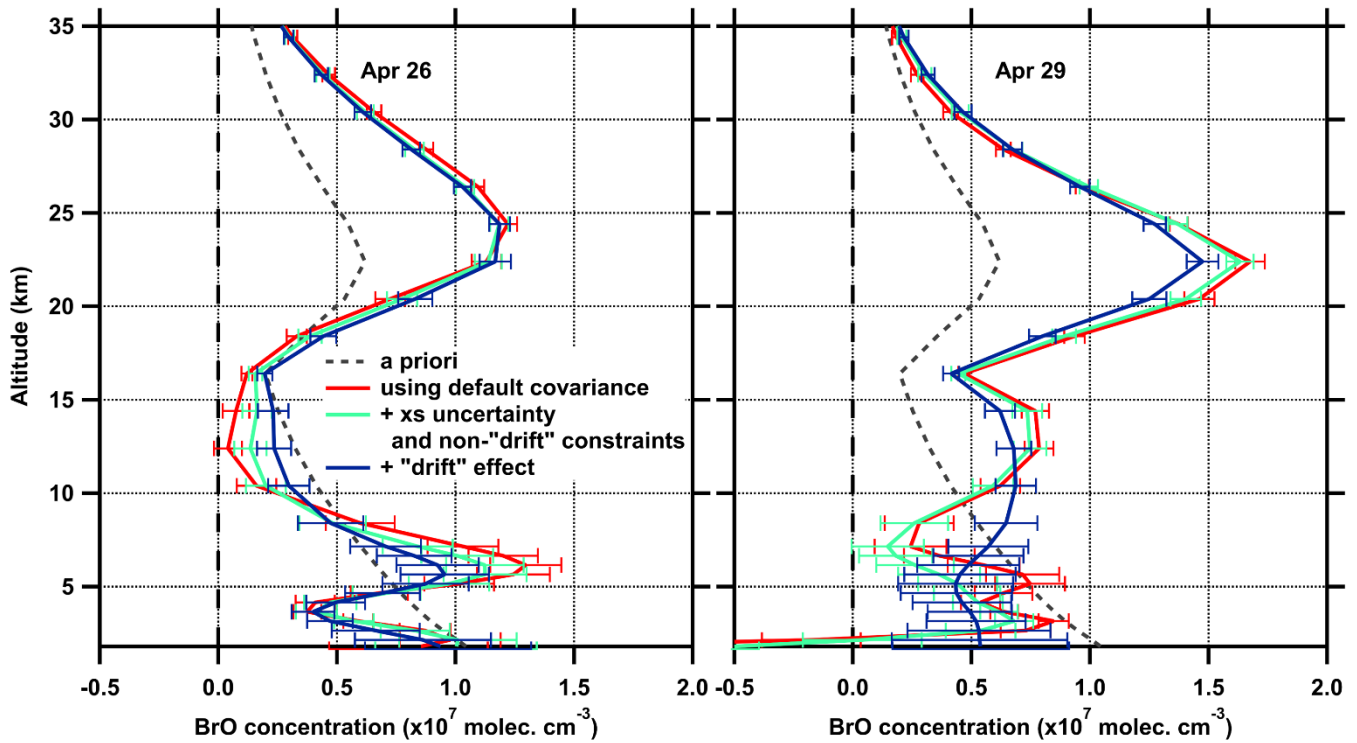
Figure S9: Sensitivity studies including additional uncertainties in the measurement covariance for retrieval

Left April 26, right April 29. In red, the default retrieval using the BrO fit uncertainty from the DOAS fitting. In pale green, additionally accounting for the uncertainty in the BrO cross-section and the O_4, NO_2, and non-"drift" component of the HCHO constraints (all added in quadrature). In dark blue further accounting for the HCHO "drift".
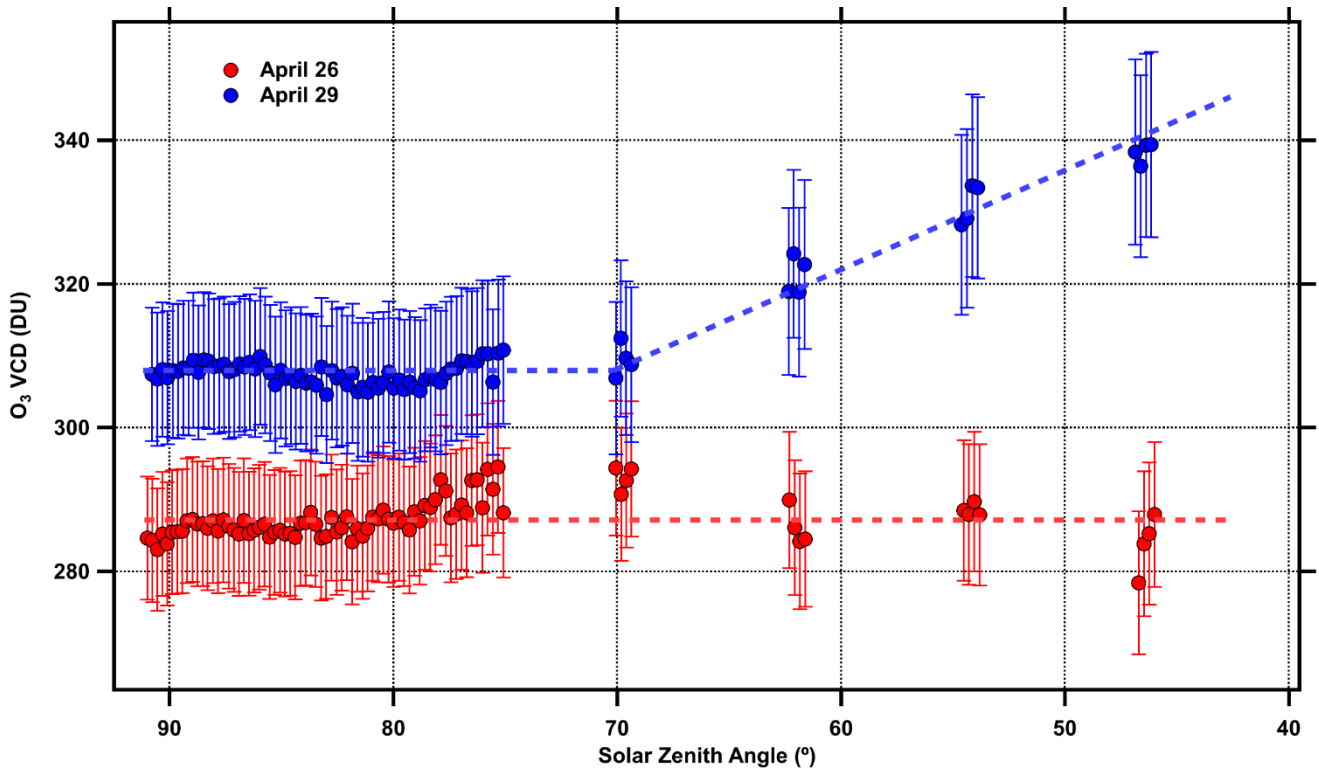
340

Figure S10: Single-spectrum O$_3$ VCD retrievals for MT-DOAS ZS data

Points show O$_3$ VCDs retrieved from individual one-minute spectra. Lines are used to guide the eye to the time-dependence retrieved for use in in the time-dependent retrieval which is referenced to SZA = 70°. The actual function used is in time which maps roughly linearly to SZA over this range but which obscures that the change in trend occurs at SZA = 70°.
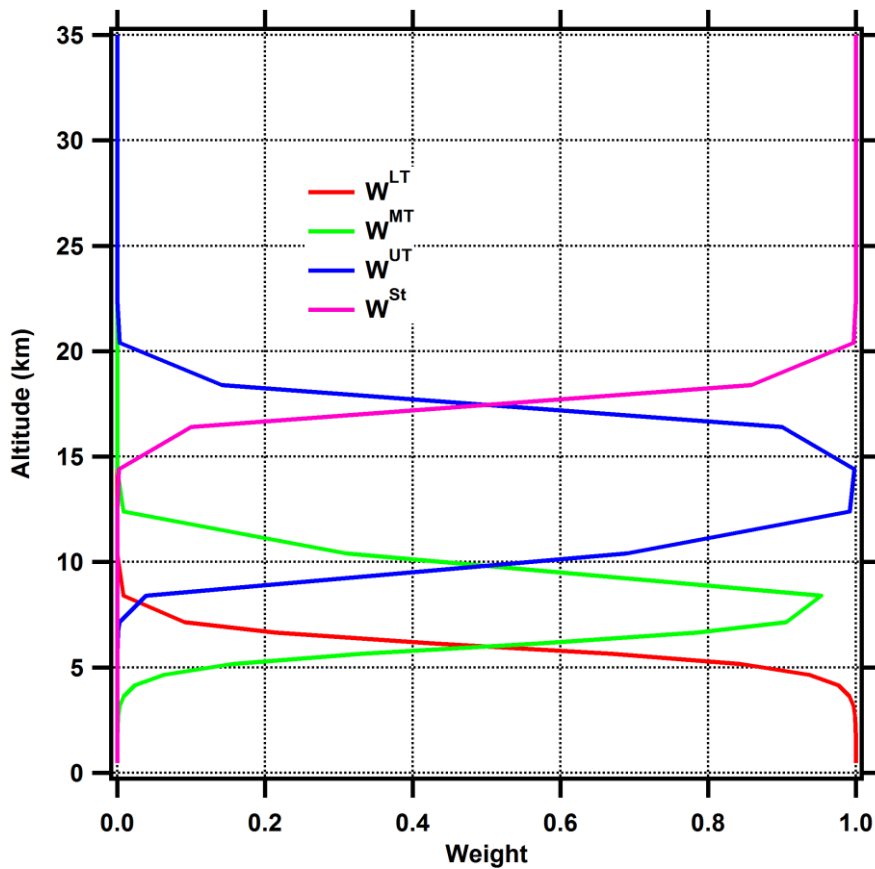
345

Figure S11: Altitude weights (W^L) used to define atmospheric layers L for time-dependent retrieval

On the basis of CAM-Chem trends four atmospheric layers are defined: the lower troposphere (LT; 0 – 6 km) middle troposphere (MT; 6- 10 km), upper troposphere (UT; 10 – 17.5 km), and stratosphere (St; > 17.5 km). All layers are defined to transition exponentially at the edges with 1/e heights of 0.5 km. They are further normalized such that the sum of all weights is 1 for all altitudes.
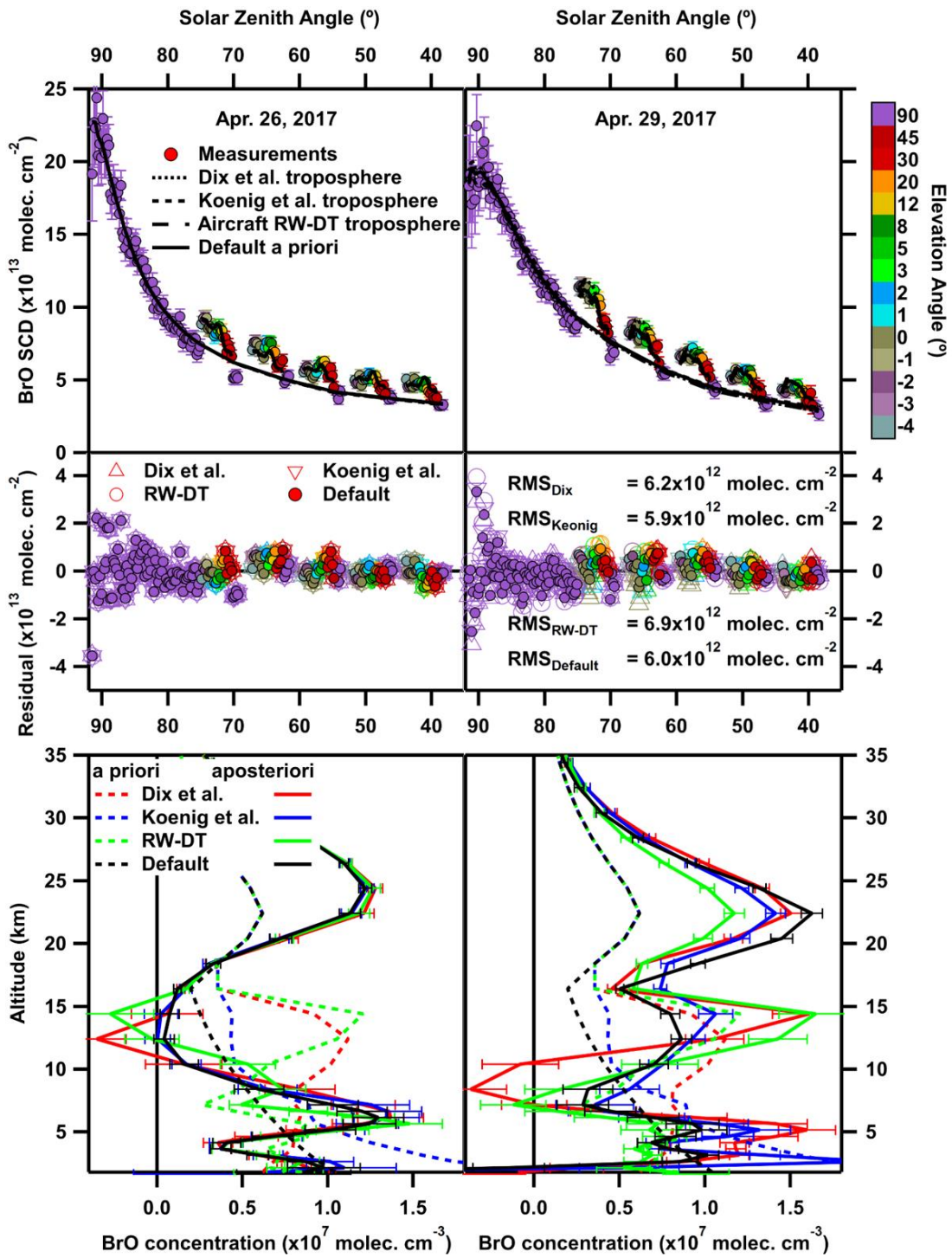
350

Figure S12: Profile a priori sensitivity studies for BrO

Sensitivity studies feed four tropospheric profiles through the time-dependent BrO retrieval: the average BrO profile from the eastern Pacific (Dix et al., 2016), from the western Pacific (Koenig et al., 2017), using the RW-DT aircraft profile reported in this work, and the default constant mixing ratio of 0.5 pptv. Top: Reproduction of measured BrO SCDs. Differences when using different a priori profiles are generally imperceptible with the exception of the eastern Pacific profile for select MAX scans on April 29. Middle: Retrieval residuals, for April 26, differences in residuals are extremely minor and the RMS residual is 6.2×10^{12} molec. cm^{-2} for all a priori profiles. The RMS residual using the western Pacific a priori is slightly better than using the default a priori. Bottom: retrieved BrO profiles. Dashed lines are a priori profiles, solid lines corresponding a posteriori. The retrieved profile on April 26 is largely insensitive to a priori apart from in the vicinity of the tropopause. On both days, the western Pacific a priori gives results similar to the default, however, it is not used due to being very swingy on April 29.
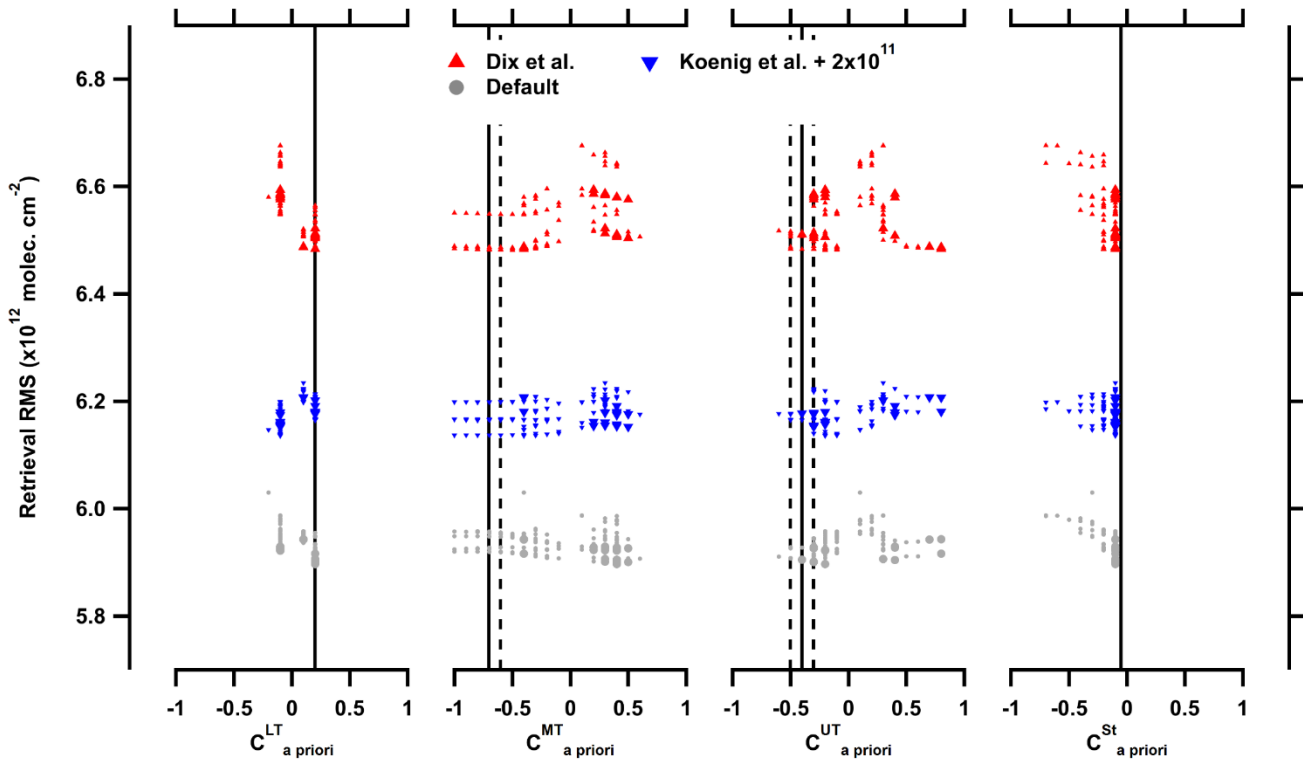
Figure S13: Time-dependent scaling factors (C^L) a priori sensitivity studies for BrO

Sensitivity studies feed three a priori profiles through the time-dependent profile retrieval and further use all permutations of a prior values for the scaling factors C^L on [-1, 1] sampled every 0.1. A priori values of zero were found to produce mathematical singularities even when for only one element of C^L. Displayed data are filtered for the condition that the retrieved partial columns in all layers L vary by less than 2×10^{13} molec. cm^{-2} among the a priori profiles used. The twenty sets of values for which the differences in partial columns were least are shown with larger symbols. Based on this and trends against RMS $C^{LT} = 0.2$ and $C^{St} = -0.1$ were selected. Rather than select the best setting on this criterion alone, sensitivity to small changes in the a priori C^L was further examined. Based on this criterion six settings were identified on $C^{MT} \in [-0.7, -0.6]$ and $C^{UT} \in [-0.5, -0.3]$. From this set the settings with the lowest RMS using the default a priori profile was selected as indicated by the solid black lines. Dashed lines indicate the remainder of the set with similar results. C^{St} was subsequently adjusted to 0.05 rather than 0.1.
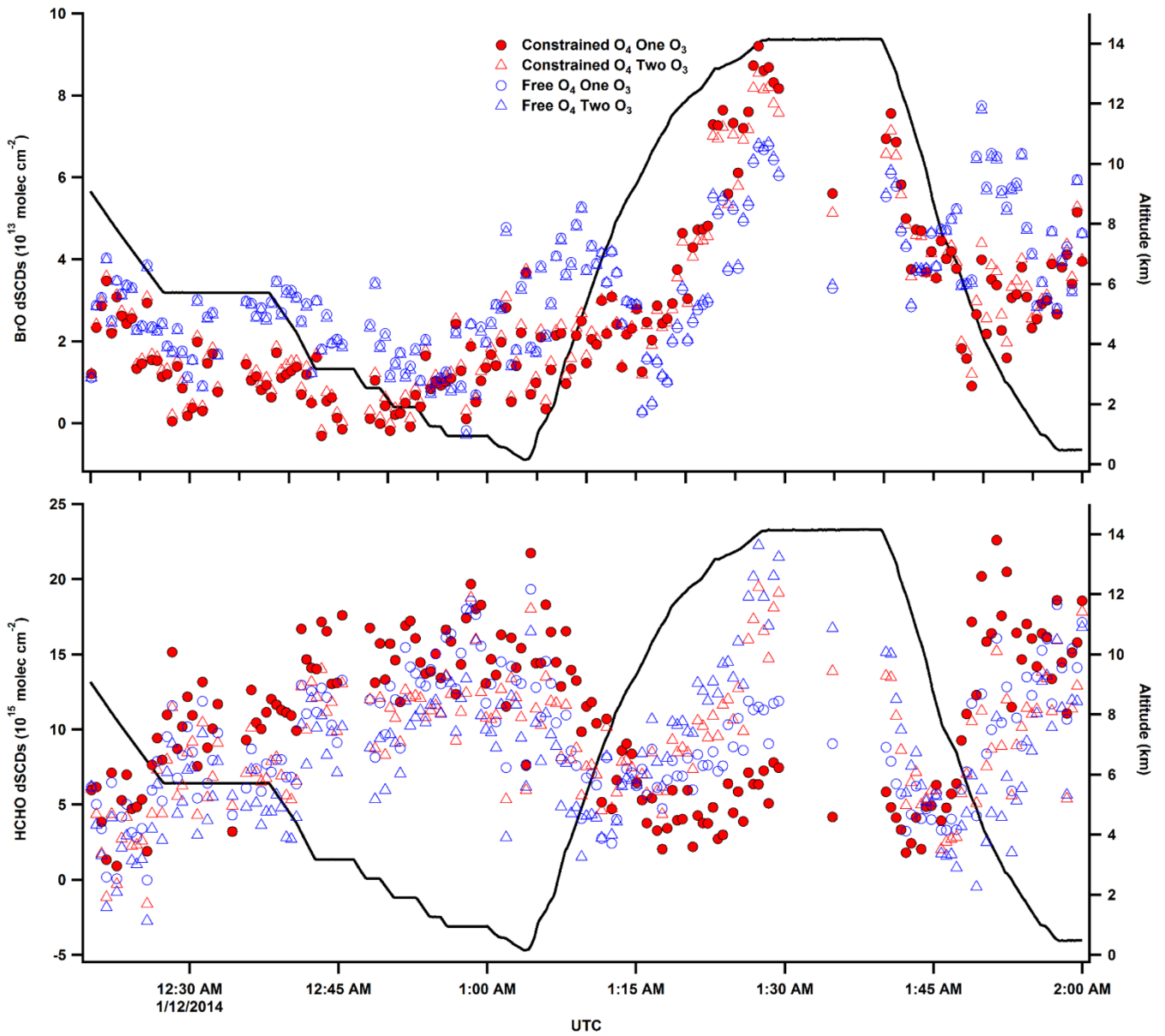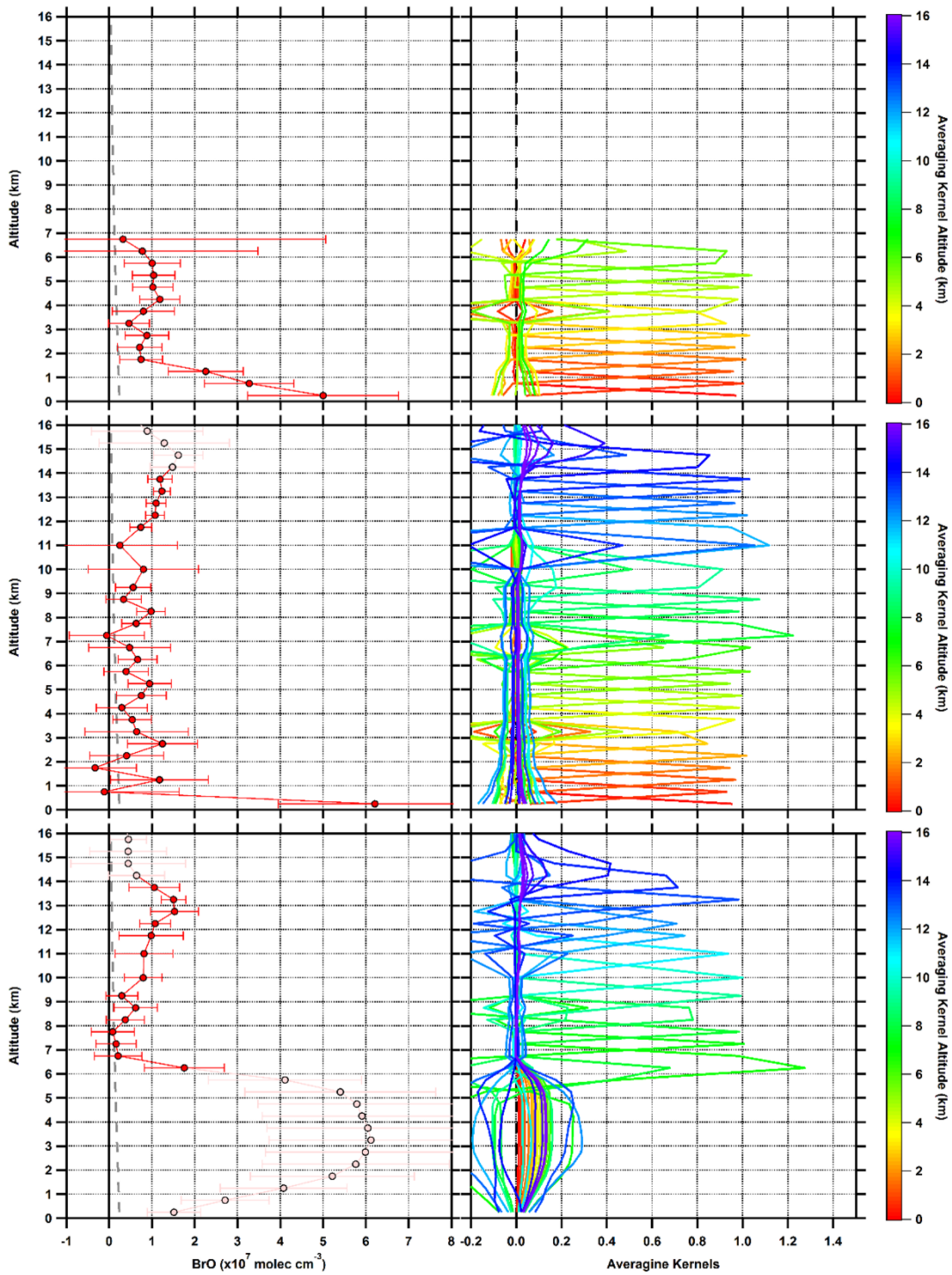
29

Figure S14: BrO and HCHO fit sensitivity studies for CONTRAST RF01 RW-DT profiles

Sensitivity studies for BrO (top) and HCHO (bottom) varying the constraint of O_4 and the inclusion of a second O_3 cross-section at 243 K in addition to the 223K cross-section.

Figure S15: BrO profile retrievals for individual component profiles during CONTRAST RF01 RW-DT

From top to bottom BrO retrievals for RF01-06, -07, and -08. Points in red are selected for inclusion in the overall average profile based on significant AVK while pink points are outputs from the retrieval which are excluded from the average due to limited information content.

385
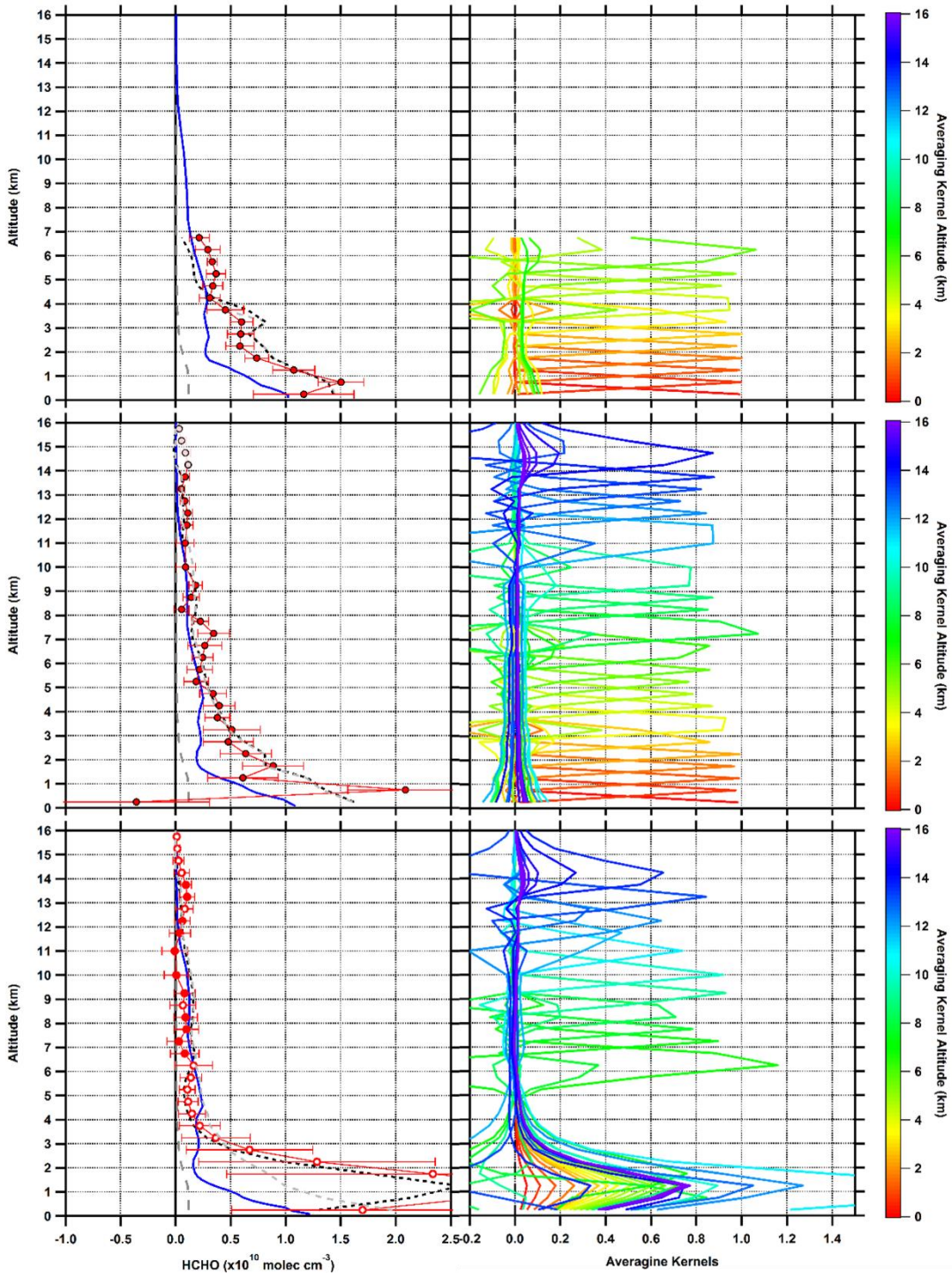
390

Figure S15: HCHO profile retrievals for individual component profiles during CONTRAST RF01 RW-DT

From top to bottom HCHO retrievals for RF01-06, -07, and -08. Points in red are selected for inclusion in the overall average profile based on significant AVK while white points are outputs from the retrieval which are excluded from the average due to limited information content. Results are compared to measurements by ISAF with the retrieved AVK applied (dashed black lines) and with the model predictions from CAM-Chem.

395

34